Journal of Materials Chemistry A

Low temperature pseudomorphic synthesis of nanocrystalline carbide aerogels for electrocatalysis

Journal:	*Journal of Materials Chemistry A*
Manuscript ID:	TA-COM-01-2015-000427.R1
Article Type:	Communication
Date Submitted by the Author:	16-Apr-2015

Complete List of Authors:	Chen, Ke; Henan University, Huang, Xiaowei; Henan University, Zhang, Zhuoxi; Henan university, DU, Ai; Shanghai Key Laboratory of Special Artificial Microstructure Materials and Technology, Pohl Institute of Solid State Physics, Tongji University, Shanghai 200092, China, Zhou, Bin; Shanghai Key Laboratory of Special Artificial Microstructure Materials and Technology, Tongji University, Xu, Yin; Henan Polytechnic University, Zhou, Zheng-Ji; Henan University, The Key Laboratory for Special Functional Materials of the MOE Wang, Yongqiang; Henan University,

Journal of Materials Chemistry A RSCPublishing

COMMUNICATION

Low temperature pseudomorphic synthesis of nanocrystalline carbide aerogels for electrocatalysis

Cite this: DOI: 10.1039/x0xx00000x

Ke Chen, [a] Xiaowei Huang, [a] Zhuoxi Zhang, [a] Ai Du, [b] Bin Zhou, [b] Yin Xu, [c] Zhengji Zhou, [a] Yongqiang Wang [a]

Received 00th January 2012,
Accepted 00th January 2012

DOI: 10.1039/x0xx00000x

www.rsc.org/

Here we demonstrate a low-temperature pseudomorphic transformation of carbide aerogels for electrocatalysis. The sustaining temperature-gradient-driving transportation of volatile metal compound and carbon diffusion-limited growth yield highly-active, mesoporous, nanocrystalline TiC and NbC aerogels with high surface areas (265 and 159 m^2/g) and porosities (~83 and 80 vol%) from carbon aerogels, respectively.

Introduction

Due to their low density, high surface area, and open-celled porous structures, aerogels have potential applications such as thermal and acoustic insulation, outer-space particle capture, energy storage, sensors, catalysis, inertial confinement fusion (ICF) and many more[1, 2]. However, the exploration of distinctive and diverse properties of aerogels has been limited because of their low crystallinity. In the sol-gel process involved by the preparation of traditional aerogels (*e. g.* SiO_2, Al_2O_3), the hydrolysis and condensation of metal compound precursors form amorphous gels at low temperature[3]. For crystallization, further high-temperature calcination renders aerogels the melting of sold phases, collapse of porous frameworks, and crack of macroscopic solids[4]. With the growing requirements in special functional porous materials, crystalline aerogels have been recently attracting much attention. One of strategies is the assembly of surface functionalized nanocrystals as building blocks into the three-dimensional connected networks by polymerization, followed by a supercritical drying process. However, the compositions of aerogels are still limited to metal chalcogenides (CdSe, PbS)[5], noble metals (Au, Ag, AgAu)[6], transitional metal oxides (ZnO, SnO_2)[7] and perovskite oxides ($BaTiO_3$)[8], because of the demanded colloidal forming process.

In the recent years, the thermal conversion of oxide aerogel precursors has been an alternative strategy for preparing self-replicated and polycrystalline metal, carbide, silicon, and nitride aerogels without direct sol-gel process[9, 10]. Owing to the excellent thermal properties and high oxidation stabilities, SiC aerogels have recently received special attention[11], which also pave a way for preparing other highly porous carbides (*e. g.* TiC, NbC, TaC, WC) for thermally insulator, catalyst carriers, energy storage and conversion, as well as backlight ICF targets in high-temperature plasma experiments[12]. Generally, monolithic carbide aerogels can be synthesized by carbothermal reduction of metal oxides with carbon at high temperature (higher than 1400 °C). These processes are cost-intensive and time-consuming (>24h). And the morphologic control of carbide aerogels is also difficult due to the various crystal-growth tendencies of carbides at high temperature[13].

Herein, we have demonstrated a low-temperature pseudomorphic synthesis approach for directly converting carbon aerogels into highly porous, polycrystalline titanium (niobium) carbide aerogels, thus following a solid-gas-solid reaction mechanism between metal Ti (Nb) with C in aid of iodine catalysts. Neither highly pure protective atmosphere

(*e.g.* Ar) nor special heating system (>1200 °C) is necessary, which is straightforward and energy-efficient. More importantly, this comprises a general synthetic strategy for different kinds of carbide aerogels and nanoporous structures for electrocatalytic applications.

Results and discussion

Carbon aerogels have been utilized as templates to synthesize TiC and NbC aerogels by a low-temperature pseudomorphic transformation following a solid-gas-solid mechanism, which is schemed in Fig. 1. Prior to the transformation, monolithic carbon aerogel plates are synthesized by the base-catalysed (sodium carbonate) gelation and subsequent carbonization of resorcinol and formaldehyde in deionized water, followed by a simple activation with CO_2 at 1000 °C. The carbon aerogels are of an openly porous 3D disorder framework, which is suitable for highly efficient absorption and decomposition of the gaseous metal iodides to yield TiC and NbC at a relatively low temperature, respectively.

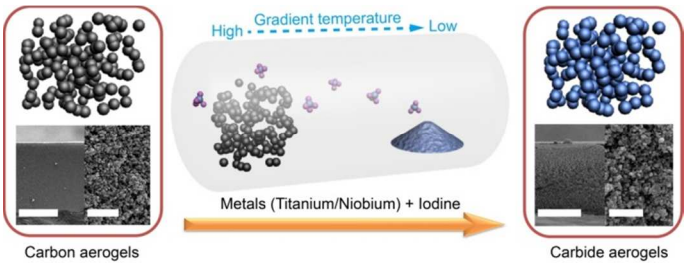

Fig. 1 Schematic of the synthetic process of TiC and NbC aerogels. Scale bar: 500 μm, 1 μm, 500 μm, and 1 μm from left to right.

After reaction, the products show the similar morphology to carbon templates, without losing the porous framework (Fig. 2a-c). EDS analyses (Fig. 2d-e) show that the converted products mainly contain Ti and C elements, as well as Nb and C elements, respectively. A little detected sign of I element could be contributed to absorbed I_2 at the surface of carbide aerogels. By the XRD analyses (Fig. 2f), the crystalline phases are presented in the products after reaction, which are distinct from the amorphous phases of carbon aerogels[14]. The peaks located at 36.0°, 41.8°, 60.6°, 72.5°and 76.3° have been indexed as the (111), (200), (220), (311), and (222) diffractions of cubic TiC (JCPDS No.65-8808), respectively. Analogously, the peaks located at 34.8°, 40.6°, 58.7°, 70.0°, and 73.7°, are corresponding to the (111), (200), (220) , (311), and (222) diffractions of cubic NbC (JCPDS No.65-8784), respectively. Both diffraction peaks in XRD patterns of polycrystalline carbide products are broader than those of the standard diffraction patterns, suggestive of the relatively small crystalline sizes. Calculated based on Scherrer analyses, the average crystal sizes of TiC and NbC aerogels are about 8.4 nm and 9.6 nm, respectively. With the consideration of morphology and crystallinity, the products are referred as nanocrystalline carbide (TiC and NbC) aerogels.

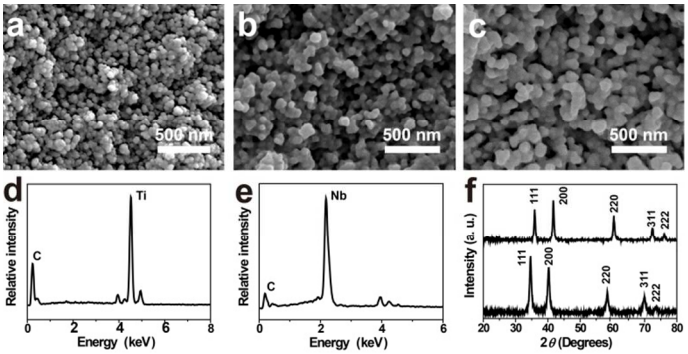

Fig. 2 SEM images (a-c), EDS analyses (d, e) and XRD patterns (f) of C, TiC and NbC aerogels.

The microstructures of TiC and NbC aerogels are further probed by SEM, TEM, and HRTEM measurements. Fig. 3a-c shows morphologic details of C, TiC and NbC aerogels, respectively. A continuous disorder network is observed in each sample, which is assembled by large amounts of nanoparticles with about 100 nm. The nanoparticles are the secondary particles, which are made of primary crystals. Both porous frameworks of TiC and NbC aerogels are well preserved after reaction, although the sizes of their secondary particles become slightly larger. The TEM image (Fig. 3d) of TiC aerogels shows that a randomly distributed nanoporous network is connected by many nanoparticles with each other, which is consistent with the observation of SEM images. Those nanoparticles are made of the primary crystals with the size of ~8 nm, as shown in the HRTEM image of TiC aerogels (Fig. 3e), in line with their XRD analyses. From the Fourier analysis (Fig. 3e inset) of the selected region in Fig 3e, the spacing of lattice fringe of single crystal is measured to be around 0.25 nm, which is in a good agreement with the parameter (0.253 nm) of the (111) plane of cubic phase TiC. Several concentric diffraction rings made of scattered points are shown in the SAED patterns of TiC aerogels (Fig. 3f). Being consistent with the analytic results of the XRD pattern, they are indexed as the Miller indices [111], [200], [220] and [311] of the diamond cubic lattice of TiC, respectively. The similar results to the analyses of TiC aerogels are also obtained. The NbC aerogels maintain the openly porous structures (Fig. 3g), the crystalline size of which is about 9 nm (Fig. 3h). Their SAED patterns are also indexed as the Miller indices [111], [200], [220] and [311] of the diamond cubic lattice of NbC, respectively.

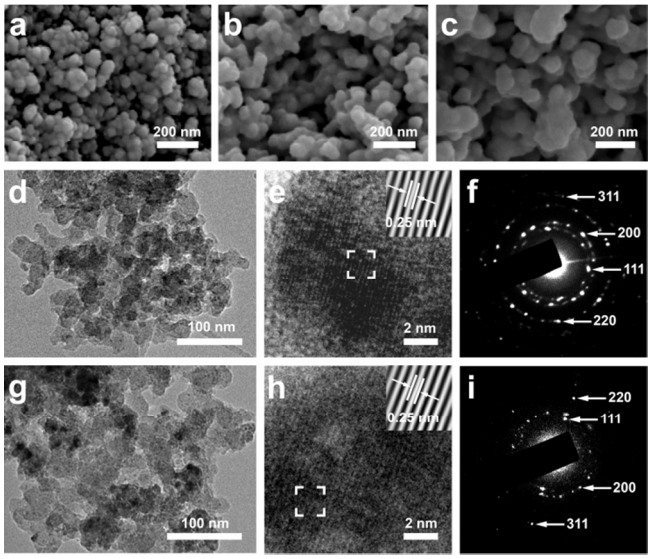

Fig. 3 SEM images of C (a), TiC (b) and NbC (c) aerogels; TEM images (d, g), HRTEM images (e, h) and SAED patterns (f, i) of TiC and NbC aerogels. Insets: Fourier filtering images of details in (e) and (h).

The surface and pore-size characterization of carbide aerogels is performed by nitrogen adsorption/desorption analysis. Both isotherms for TiC and NbC aerogels, as shown in Fig. 4a, show the details of the low-pressure and high-pressure regions in which micropore and mesopore filling occurs, respectively. They reveal both H1 and H4 hysteresis loops (the International Union of Pure and Applied Chemistry classification), which are characteristic of an interconnected hierarchical pore system. As comparison, the isotherm of C aerogels mainly shows H1 hysteresis loops, suggestive of the presence of micropores. The TiC and NbC aerogels possess the BET specific surface area (SSA) as high as 265 and 159 m^2/g, respectively, which are larger than those of traditional porous TiC and NbC (<50 m^2/g)[15, 16]. The comparison of characteristics of C, TiC and NbC aerogels is listed in Table 1. Taking into consideration atomic weights of metal and carbon, the molar BET SSAs of TiC and NbC aerogels are calculated, which are comparable to that of carbon aerogels. Fig. 4b displays the data of pore size analysis from nitrogen adsorption by applying a nonlocal density functional theory (NLDFT). The pore size/volume distribution indicates that TiC and NbC aerogels are hierarchically porous and distinctive due to the existence of well-defined micropores and mesopores, which are corresponding with the observation of SEM and TEM images. Both porosities of TiC and NbC aerogels are close to that of carbon aerogels, although their micropore volumes become smaller. It should be explained that decomposition of Ti/Nb-iodine on carbon and the subsequent diffusion of carbon atoms into metal Ti/Nb brings the changes for aerogel frameworks, thus leads to the filling, compression and coalescence of micropores, as well as the formation of new mesopores.

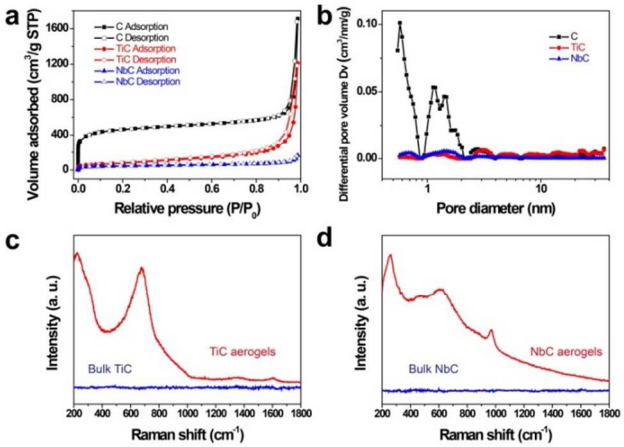

Fig. 4 Nitrogen adsorption/desorption isotherms (a) and pore size distribution (b) of C, TiC and NbC aerogels; Raman spectra of TiC (c) and NbC (d) aerogels.

The unique spectroscopic properties of TiC and NbC aerogels are performed by Raman analyses. The Raman spectrum (Fig. 4c) of TiC aerogels shows three peaks near 260, 412, and 615 cm^{-1}, respectively, which are consistent with the reported results about TiC with defects[17]. In contrast, the bulk cubic TiC has no Raman active vibrational modes[18]. The presence of first order Raman scattering should be induced by the carbon vacancies, surface defects from TiC aerogels. Evidenced by the presence of D band and G band near 1350 and 1580 cm^{-1} from its Raman spectrum, respectively, a little signal of sp^2 carbon in converted TiC could be related with the trace amounts of unreacted carbon or graphene-like carbon catalytically produced on TiC. Similar phenomenon is also observed in Raman spectrum (Fig. 4d) of NbC aerogels. The peaks at 257, 622, and 980 cm^{-1} could be also contributed to the defect-induced first-order Raman scattering from NbC aerogels[19]. In the indirect-drive ICF experiments, energy losses of target materials, mainly induced by stimulated Raman/Brillouin scattering processes, must be effectively controlled to achieve the required radiation drive and symmetry[20]. Accordingly, the unique Raman scattering properties of TiC and NbC aerogels may be conducive to the direct scaling and control of the instabilities induced by those energy losses.

Based on the theory of thermodynamics, metal Ti and Nb powders can react with iodine to form gaseous Ti-iodine and Nb-iodine complexes. Then, the complexes diffuse to the surface of carbon aerogel frameworks and homogeneously react with carbon to form carbides. The reaction could be described as the following equations:

Table 1 The related parameters with physical properties of C, TiC and NbC aerogels.

Aerogels	Bulk density[a] (g•cm^{-3})	Skeletal density[b] (g•cm^{-3})	BET specific surface area (m^{2}g^{-1}/m^{2}mol^{-1})	Micropore surface area (m^{2}g^{-1}/m^{2}mol^{-1})	Total Pore volume[c] (cm^{3}g^{-1})	Micropore volume (cm^{3}g^{-1})	Porosity[d] (vol%)
C	0.13	2.11	1758/21096	1436/17232	2.65	0.59	93.84
TiC	0.73	4.39	265/15876	136/8147	1.37	0.05	83.37
NbC	1.35	6.54	159/16842	81/8580	0.81	0.03	79.36

a: ρ_b is measured by weight method, average of 3 samples; *b*: ρ_s is obtained from helium pycnometry; *c*: V_{total} was calculated by the single-point adsorption method; *d*: Porosity is calculated via $\Pi = 1 - \rho_b / \rho_s$.

$$Ti\ (Nb)\ (s) + 2I_2\ (s, g) \rightleftarrows TiI_4\ (NbI_4)\ (g) \quad (1)$$

$$TiI_4\ (NbI_4)\ (g) + C\ (s) \rightarrow TiC\ (NbC)\ (s) + 2I_2\ (s, g) \quad (2)$$

Take TiC as an example, during the primary process, the reaction in equation (1) is exothermic and it is facile to the reaction of metal Ti with iodine at low temperature (~200 °C). When the temperature climbs to a higher value (~400 °C), the abundant gaseous TiI_4 is liberated from Ti sources, and a reverse reaction could occur. The temperature gradient can drive to the transport of Ti species. At the higher temperature region (above 500 °C), the gaseous TiI_4 can decompose into the deposited Ti on the surface of carbon particles. According to the available thermodynamic data[21], both strand free energies for the formation of TiC and NbC are calculated to be negative (~ -170 and -130 kJ/mol), predicting a spontaneous reaction and sufficient driving force for the whole reaction process in equation (2). While the diffusion of carbon in metal carbide is much easier than that of metal, TiC layers should grow by the diffusion of carbon. The diffusion efficiency of carbon could be determined by temperature, according to a diffusion-controlled layer growth mechanism[21]. In order to confirm the effect of temperature on carbon diffusion, we conducted XRD characterization of products after reaction from 500 to 900 °C for 6h (Fig. S1†). An empirical lowest temperature about 550 °C is required for the successful conversion of the carbon aerogels, where TiC crystals are presented and their crystalline sizes increase with the rising temperature. At a certain temperature of carbon activation, the thickness (component) of TiC layers increases with the reaction time. While the signals of unreacted amorphous carbon are still detected from the XRD and TEM analyses of products, even if the reaction time is lengthened to 24h (Fig. S2†). Therefore, by rising the temperature to improve reaction rate of carbides, a TiC skeleton can be almost completely converted from carbon phases under the sustaining transport of the reactive Ti species (enough reaction time). Note that the unique nature of carbon aerogels is also facile to the primary formation and subsequent diffusion-limited uniform growth of carbide layers, such as the large exposed surface areas, nanometer grain sizes and high-density grain boundaries.

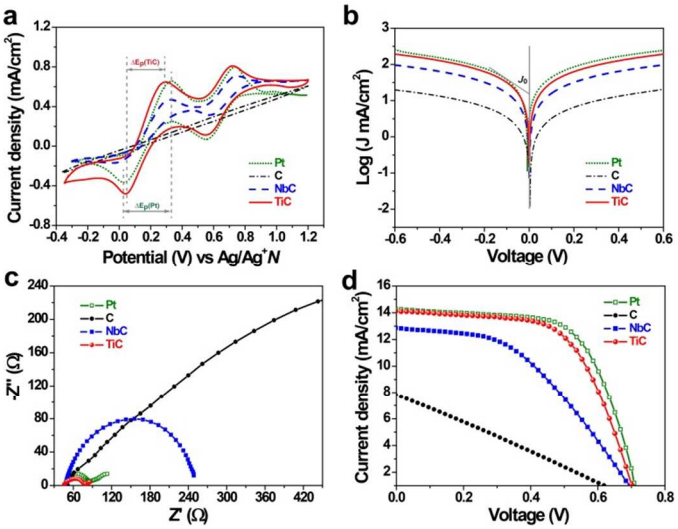

Fig. 5 Electrocatalytic properties of TiC and NbC aerogels. Cyclic voltammograms (a), Nyquist plots (b), and Tafel polarization curves (c) of TiC, NbC, C aerogel and Pt catalysts for I_3^-/I^- species. *J-V* curves (d) for DSSCs with TiC, NbC, C and Pt CEs.

Due to their highly efficient reduction of I_3^- to I^- in the electrolyte, TiC and NbC catalysts have been proposed to replace the expensive Pt as counter electrodes (CEs) in dye-sensitized solar cells (DSSCs)[22]. To investigate their catalytic activities, cycle voltammograms (CV), Tafel polarization, and electrochemical impedance spectroscopy (EIS) of the synthesized TiC and NbC aerogels are measured for I_3^-/I^- species, respectively. Compared with those of NbC aerogels, the redox peaks of TiC aerogels at low potential (< 0.5 V) in their CV curves (Fig. 5a) exhibit a higher current density, even beyond those of Pt, which can be attributed to the redox reaction between I_3^- and I^- species. In contrast, no obvious redox peaks are presented for C aerogels. Besides, the peak-to-peak separation (ΔE_p) for TiC aerogels is smaller than those for Pt and NbC, suggestive of their high charge transfer rate. These indicate that TiC aerogels have excellent catalytic activity. The Tafel curves (Fig. 5b) of TiC aerogels also

exhibit the large exchange current density (J_0) comparable to that of Pt, suggestive of superior catalytic activity for I_3^- reduction. In contrast, the lower J_0 for C aerogels indicates that C aerogels cannot outperform TiC and NbC aerogels for catalyzing I_3^- reduction. The Nyquist plot (Fig. 5c) of TiC aerogels shows a similar charge transfer resistance (R_{ct}) to that of Pt, which is much lower than those of NbC and C aerogels (Fig. S3†). The low R_{ct} of TiC aerogel electrode indicates their high J_0, and the change tendency of R_{ct} for all electrodes is generally in accordance with that of J_0 presented in their Tafel curves. The photocurrent density-voltage (*J-V*) curves (Fig. 5d) for DSSCs with TiC, NbC, C aerogels and Pt CEs are also measured to evaluate the photovoltaic performance. The photovoltaic and electrochemical parameters for various electrodes are listed in supplementary Table S1. † The DSSCs with TiC CEs give a high power conversion (PCE) of 6.1%, which is comparable to that of DSSCs with a Pt CE and much higher than those of DSSCs with NbC (4.1%) and C (1.4%) aerogel CEs. The photovoltaic performance indicates the high catalytic activity of TiC aerogels as CEs for I_3^- reduction in DSSCs, which is in agreement with their CV, Tafel polarization and EIS results. In addition, the electrocatalytic properties (Fig. S4†) of TiC and NbC aerogel electrodes for hydrogen evolution reaction (HER) are also probed, since IV-VI transition metal carbides can be explored for electrochemical water splitting[23]. Surprisingly, the relatively low Tafel slop b (128 mV/dec) and onset potential η (290 mV) are achieved for TiC/C aerogel electrodes with enhanced electrocatalytic activity, although the relatively poor HER activities are obtained for TiC and NbC aerogel electrodes (b > 300 mV/dec; η > 400 mV). It could be attributed to the synergetic effect between TiC and C catalysts[23], which should be considered for developing new, low-cost, high-efficiency catalysts.

Conclusions

We have provided a low-temperature pseudomorphic synthesis strategy for preparing TiC and NbC aerogels from C templates (aerogels). Together with the unique structural nature of carbon aerogels, the temperature controlled transportation of volatile Ti- and Nb- iodine complexes and diffusion-limited layer growth play a key role in the successful conversion. The TiC and NbC aerogels retain the similar porous morphologies to the original templates, due to the low volatility of carbon and carbide solids during the reaction process. Unusually, they possess the higher BET surface areas and lower bulk densities than previous porous carbides, as well as the one-order Raman activities. In addition, more efforts have been also devoted to assemble the carbide aerogels into electrocatalytic electrodes and evaluate their application potential for DSSCs and HER. TiC aerogels show an excellent electrocatalytic activity for I_3^-/I^- species, which is comparable to Pt and outperform NbC and C aerogels. Based on the thermodynamic process of TiC and NbC aerogels, the proposed route might be used to prepare other carbide (*e. g.* WC, MoC) aerogels as economical, highly-active catalysts from carbon aerogels under the relatively milder conditions.

Acknowledgements

This work was supported by the National Natural Science Foundation of China (51172163), National High Technology Research and Development Program of China (2013AA031801), the Seed Project for Young Excellent Talents of Henan University (0000A40518).

Notes and references

[a] Key Laboratory for Special Functional Materials of Ministry of Education, Henan University, Kaifeng 475004, China.
[b] Shanghai Key Laboratory of Special Microstructure Materials and Technology, Tongji University, Shanghai 200092, China.
[c] Wanfang College of Science and Technology of Henan Polytechnic University, Zhengzhou 451400, China.

† Electronic Supplementary Information (ESI) available: [The experimental details are described including synthesis, characterization methods and electrocatalytic measurements]. See DOI: 10.1039/c00000

1 J. Pollanen, J. I. A. Li, C. A. Collett, W. J. Gannon, W. P. Halperin, J. A. Sauls, *Nat. Phys.*, 2012, **8**, 317; J. Biener, M. Stadermann, M. Suss, M. A. Worsley, M. M. Biener, K. A. Rose, T. F. Baumann, *Energ. Environ. Sci.*, 2011, **4**, 656; S. Nardecchia, D. Carriazo, M. L. Ferrer, M. C. Gutierrez, F. Monte, Chem. Soc. Rev., 2013, **42**, 794; H. Sun, Z. Xu, C. Gao, *Adv. Mater.*, 2013, **25**, 2554.
2 H. F. Ju, W. L. Song, L. Z. Fan, *J. Mater. Chem. A*, 2014, **2**, 10895; H. P. Cong , X. C. Ren , P. Wang, S. H. Yu, *ACS Nano*, 2012, **6**, 2693; H. Hu, Z. Zhao, R. Zhang, Y. Bin, J. Qiu, *J. Mater. Chem. A*, 2014, **2**, 3756; O. A. Hurricane, D. A. Callahan, D. T. Casey, P. M. Celliers, C. Cerjan, E. L. Dewald, T. R. Dittrich, T. Döppner, D. E. Hinkel, L. F. Berzak Hopkins, J. L. Kline, S. Le Pape, T. Ma, A. G. MacPhee, J. L. Milovich, A. Pak, H.-S. Park, P. K. Patel, B. A. Remington, J. D. Salmonson, P. T. Springer, R. Tommasini, *Nature*, 2014, **506**, 343.
3 C. J. Brinker, C.W. Scherer. *Sol-gel Science: The Physics and Chemistry of Sol-gel Processing*, Academic Press, Boston (1990); L. Franzel, C. Wingfield, M. F. Bertino, S. Mahadik-Khanolkar, N. Leventis, *J. Mater. Chem. A*, 2013, **1**, 6021.
4 Z. Zhao, D. Chen and X. Jiao, *J. Phys. Chem. C*, 2007, **111**, 18738.
5 J. L. Mohanan, I. U. Arachchige, S. L. Brock, *Science*, 2005, **307**, 397; I. U. Arachchige, S. L. Brock, *Acc. Chem. Res.*, 2007, **40**, 801; S. Bag, P. N. Trikalitis, P. J. Chupas, G. S. Armatas, M. G. Kanatzidis, *Science*, 2007, **317**, 490.
6 N. C. Bigall, A. -K. Herrmann, M. Vogel, M. Rose, P. Simon, W. Carrillo-Cabrera, D. Dorfs, S. Kaskel, N. Gaponik, and A. Eychmuller, *Angew. Chem. Int. Ed.*, 2009, **48**, 9731; V. Lesnyak, A. Wolf, A. Dubavik, L. Borchardt, S. V. Voitekhovich, N. Gaponik, S. Kaskel, A. Eychmüller, *J. Am. Chem. Soc.*, 2011, **133**, 13413.
7 T. E. Baumann, S. O. Kucheyev, A. E. Gash and J. H. Satcher Jr., *Adv. Mater.*, 2005, **17**, 1546; Y. Gao, C. N. Sisk and L. J. Hope-Weeks, *Chem. Mater.*, 2007, **19**, 6007.

8 F. Rechberger, F. J. Heiligtag, M. J. Suess, M. Niederberger, *Angew. Chem. Int. Ed.*, 2014, **53**, 6823.
9 N. Leventis, N. Chandrasekaran, A. G. Sadekar, C. Sotiriou-Leventis, H. Lu, *J. Am. Chem. Soc.*, 2009, **131**, 4576; N. Leventis, N. Chandrasekaran, A. G. Sadekar, S. Mulik, C. Sotiriou-Leventis, *J. Mater. Chem.*, 2010, **20**, 7456; M. Rousseas, A. P. Goldstein, W. Mickelson, M. A. Worsley, L. Woo, A. Zettl, *ACS Nano*, 2013, **7**, 8540.
10 K. Chen, Z. Bao, A. Du, X. Zhu, G. Wu, J. Shen, B. Zhou, *Micropor. Mesopor. Mater.*, 2012, **149**, 16; K. Chen, Z. Bao, J. Shen, G. Wu, B. Zhou, K. H. Sandhage, *J. Mater. Chem.*, 2012, **22**, 16196.
11 N. Leventis, A. Sadekar, N. Chandrasekaran, C. Sotiriou-Leventis, *Chem. Mater.*, 2010, **22**, 2790.
12 J. He, N. W. Duffyc, J. M. Pringle, Y. B. Cheng, *Electrochimica Acta*, 2013, **105**, 275; M. R. Lukatskaya, O. Mashtalir, C. E. Ren, Y. D. Agnese, P. Rozier, P. L. Taberna, M. Naguib, P. Simon, M. W. Barsoum, Y. Gogotsi, *Science*, 2013, **341**, 1502; S. J. Zenobia, R. F. Radel, B. B. Cipiti, G. L. Kulcinsk, *J. Nucl. Mater.*, 2009, **389**, 213.
13 C. N. R. Rao, F. L. Deepak, G. Gundiah, A. Govindaraj, *Prog. Solid State Chem.*, 2003, 31, 5; J. Parmentier, J. Patarin, J. Dentzer, C. Vix-Guterl, *Ceram. Int.*, 2002, **28**, 1.
14 Z. Xu, D. Cai, Z. Hu, L. Gan, *Micropor. Mesopor. Mater.*, 2014, **195**, 36.
15 Y. Shin, X. S. Li, C. Wang, J. R. Coleman, G. J. Exarhos, *Adv. Mater.*, 2004, **16**, 1212.
16 H. S. Kim, G. Bugli, G. Djega-Mariadassou, *J. Solid State Chem.*, 1999, **142**, 100.
17 M. V. Klein, J. A. Holy, and W. S. Williams, *Phys. Rev. B*, 1978, **17**, 1546.
18 M. Amer, M. W. Barsoum, T. El-Raghy, I. Weiss, S. Leclair, and D. Liptak, *J. Appl. Phys.*, 1998, **84**, 5817.
19 W. Spengler and R. Kaiser, *Solid State Commun.*, 1976, **18**, 881.
20 J. D. Lindl, R. L. McCrory, E. M. Campbell, *Phys. Today*, 1992, **45**, 32.
21 I. Barin and G. Platzki, *Thermochemical Data of Pure Substances*, Wiley-VCH Verlag GmbH, Weinheim, Germany, 1995; T. C. Wallace, D. P. Butt, *The Chemistry of Transition Metal Carbides and Nitrides*, Chapman&Hall, New York, 1996.
22 M. Wu, X. Lin, Y. Wang, L. Wang, W. Guo, D. Qi, X. Peng, A. Hagfeldt, M. Gratzel, T. Ma, *J. Am. Chem. Soc.*, 2012, **134**, 3419; H. Zhou, Y. Shi, D. Qin, J. An, L. Chu, C. Wang, Y. Wang, W. Guo, L. Wang, T. Ma, *J. Mater. Chem. A,* 2013, **1**, 3932.
23 P. Xiao, X. Ge, H. Wang, Z. Liu, A. Fisher, X. Wang, *Adv. Function. Mater.*, 2015, **25**, 1520; Y. Yan, L. Zhang, X. Qi, H. Song, J. Y. Wang, H. Zhang, X. Wang, *Small*, 2012, **8**, 3350; B. Xia, Y. Yan, X. Wang, X. W. D. Lou, *Mater. Horiz.*, 2014, **1**, 379.

The low-temperature pseudomorphic transformation of nanocrystalline TiC (NbC) aerogels with high surface areas and elctrocatalytic activities is realized for DSSCs and HER.